Ferromagnetic semiconductor and strain-switchable metal–insulator transition in $Mo_{12}S_9I_9$ nanowires

Zhantong Liu(刘展彤)[1], Huaihong Guo(郭怀红)[1,†], Kai Wang(王凯)[1], Heting Zhao(赵贺霆)[1], Miao Zhang(张淼)[1], Kexin Zhou(周可心)[1], Bo Zhao(赵波)[1], and Ye Zhang(张也)[2,3,4]

[1] *Liaoning Provincial Key Laboratory of Novel Micro-Nano Functional Materials, College of Sciences, Liaoning Petrochemical University, Fushun* 113001, *China*
[2] *Shenyang National Laboratory for Materials Science, Institute of Metal Research, Chinese Academy of Sciences, Shenyang* 110016, *China*
[3] *School of Material Science and Engineering, University of Science and Technology of China, Shenyang* 110016, *China*
[4] *College of Science, Jilin University of Chemical Technology, Jilin* 132022, *China*

(Received 9 May 2026; revised manuscript received 7 July 2026; accepted manuscript online 24 July 2026)

Low-dimensional magnetic semiconductor systems remain rare but essential for realizing spintronic devices. Using first-principles calculations, we discover that MoSI nanowire is a magnetic semiconductor with multi-stability and possesses a rich strain-responsive phase diagram. An axial compressive strain induces a phase transition to a distinct metastable magnetic semiconductor phase and an easy magnetic axis swap from the perpendicular to the axial direction. Remarkably, under an axial tensile strain, the system undergoes a first-order Mott–Hubbard-like phase transition from a magnetic semiconductor into a metastable non-magnetic metal phase. This ability to reversibly switch between magnetic semiconductors with tailored anisotropy, and the strain-tunability of the Mott–Hubbard transition, underscore MoSI nanowire as a highly promising platform for adaptive nanoelectronics, strain-sensitive magneto-devices, and phase-change applications.

Keywords: MoSI nanowires, strain engineering, magnetic anisotropy energy, metal–insulator transition

PACS: 61.46.Km, 71.30.+h, 75.30.Gw

DOI: 10.1088/1674-1056/ae8fc4 **CSTR:** 32038.14.CPB.ae8fc4

1. Introduction

Understanding the ground-state properties of materials and developing strategies to control these properties via external fields represent a central frontier in modern condensed matter physics and materials science.[1–3] Among various control methods, strain engineering has emerged as a particularly powerful technique for low-dimensional materials, demonstrating remarkable effectiveness in continuously tuning properties such as band gaps, carrier mobility, and magnetism.[4–7] However, most current research focuses on continuous property modulation within a single structural phase. A more challenging frontier is to explore systems where strain can drive qualitative phase transitions starting from a stable ground state. These transitions include the loss of magnetic order, metal–insulator transitions, or the reorientation of magnetic anisotropy.[7–10] Such transitions, if realized in a reversible and non-volatile manner, could form the basis for a new class of adaptive nanoelectronics, reconfigurable spintronics, and phase-change memory devices.

In this context, quasi-one-dimensional (quasi-1D) molybdenum chalcohalide nanowires, particularly those in the Mo–S–I family, have emerged as a versatile platform due to their unique structural motif, which consists of rigid Mo_6 octahedra interconnected by flexible three sulfur atom bridges.[11–13] This architecture imparts remarkable properties, including air stability, facile dispersion, and highly anisotropic electronic transport.[14,15] A defining feature of these materials is the bistability of the Mo–S–Mo bridges. Early experimental and theoretical studies established that these bridges can adopt either acute ($\sim 90°$) or obtuse ($\sim 150°$) bond angles.[16–22] This structural flexibility gives rise to unusual mechanical properties such as accordion-like stretching.[16,17]

However, previous studies have primarily focused on smaller building blocks, such as the single-Mo_6-octahedron nanowire $Mo_6S_3I_6$,[16,17] where the limited number of bridging sites (only three S bridges) enforces a global bistability. In this case, either all bridges are bent or all are straight. In contrast, the larger $Mo_{12}S_9I_9$ nanowire contains six independent S bridges. As we will demonstrate, this increased number of bridge sites enables the emergence of long-range ordered bond-angle superstructures, such as the alternating bent-straight pattern found in phase II. Such multi-bridge cooperativity, which is absent in smaller Mo–S–I systems, serves as the structural prerequisite for the rich phase diagram and strain-switchable magnetism reported here.

Early theoretical work established that the electronic structure of MoSI nanowires is exquisitely sensitive to strain.[16] Extending this to the $Mo_{12}S_9I_9$ system, Yang *et al.* demonstrated that the bistable sulfur bridges lead to strain-tunable electronic phases, including a ferromagnetic semicon-

†Corresponding author. E-mail: hhguo@alum.imr.ac.cn

© 2026 Chinese Physical Society and IOP Publishing Ltd. All rights, including for text and data mining, AI training, and similar technologies, are reserved.

CPB Online In-Press

ducting state in certain metastable configurations.[17] Subsequent studies have explored the roles of composition, bundling effects, and valence electron concentration in modulating the properties of MoSI nanowires.[18–22] Collectively, these works demonstrate that strain-induced changes in the Mo–S–Mo bond angles can simultaneously alter the electronic band structure and magnetic ordering, revealing an intimate coupling between structural, electronic, and magnetic degrees of freedom. While this seminal work first linked structural distortions to magnetic ordering,[16–18] the magnetocrystalline anisotropy energy (MAE) — a key parameter for stabilizing long-range magnetic order in quasi-1D systems and for determining the ease of magnetization switching — has never been investigated in the MoSI nanowire systems. Moreover, the nature of the strain-induced metal–insulator transition remained ambiguous; whether it arises from simple band broadening or from a Mott–Hubbard-type correlation collapse cannot be distinguished without explicit treatment of on-site Coulomb interactions. Furthermore, the kinetic barriers separating the multiple energy minima have never been quantitatively evaluated, leaving the feasibility of strain-driven reversible switching at room temperature unknown. In this work, by including spin-orbit coupling and many-body correlations via the DFT + U method, we reveal a rich strain-driven phase diagram where compressive strain swaps the easy axis from the axial to radial direction, while tensile strain drives a first-order Mott-like transition into a nonmagnetic metal.

In this work, we address these questions through comprehensive first-principles calculations on $Mo_{12}S_9I_9$ nanowires. To avoid the complexity introduced by interwire coupling, which can alter electronic and magnetic properties as shown in bundled systems,[20] we focus on isolated nanowires. Our calculations reveal a rich strain-driven phase diagram comprising three distinct phases, which we denote as phase I ($P_{\rm I}$), the true ground state phase II ($P_{\rm II}$), and phase III ($P_{\rm III}$), corresponding to the compressed, near-equilibrium, and stretched configurations, respectively. These phases are structurally analogous to the three local minima of the total energy as a function of the axial lattice constant reported in earlier studies, namely the 'short–short' (all bridges bent), 'short–long' (mixed bent and straight), and 'long–long' (all bridges straight) bridge configurations.[17,18] Using CI-NEB calculations, we quantitatively determine the energy barriers separating these phases for the first time, revealing an asymmetric landscape. The barrier from phase I to phase II is as low as 0.10 eV, while the reverse barrier is as high as 0.36 eV, explaining the kinetic accessibility of phase II under zero-strain conditions. Remarkably, compressive strain drives the system from phase II to phase I, inducing a dramatic reorientation of the easy magnetization axis from the direction which is perpendicular to the nanowire axis to the direction which is tilted $\sim 34^\circ$ from the axial direction and significantly reducing the magnetic anisotropy energy from 10.30 μeV/Mo to 4.67 μeV/Mo. Including spin–orbit coupling (SOC) is essential to capture this strain-driven easy-axis switching and the quantitative MAE values; without SOC, these effects would be qualitatively misrepresented. In contrast, tensile strain triggers a first-order phase transition to a nonmagnetic metal (phase III, $c = 13.80$ Å), with a barrier of 0.30 eV, while the reverse barrier is 0.23 eV. This ability to reversibly switch between two distinct magnetic semiconductors and a nonmagnetic metal via a single mechanical stimulus underscores the exceptional functional versatility and multistability of $Mo_{12}S_9I_9$ nanowires. Furthermore, systematic DFT+U calculations allow us to distinguish the Stoner spin-splitting mechanism (driving ferromagnetism) from the Mott–Hubbard gap opening (driving insulation), a distinction that previous DFT studies could not resolve.

2. Computational methods

We constructed a quasi-1D nanowire with a stoichiometry of $Mo_{12}S_9I_9$. All calculations were performed within the density functional theory (DFT) framework as implemented in the Vienna *ab initio* Simulation Package (VASP) with the projector augmented-wave (PAW) method.[23–25] The electronic exchange–correlation potential was treated under the Perdew–Burke–Ernzerhof (PBE) flavor in the generalized gradient approximation (GGA).[26] A plane-wave cutoff energy of 520 eV was used. Axial strain was simulated by varying the lattice constant c along the periodic wire direction. Atomic positions were fully relaxed until the residual Hellmann–Feynman forces were below 0.01 eV/Å. A Monkhorst–Pack k-point mesh[27] of $20 \times 1 \times 1$ was used for Brillouin zone integration. The electronic self-consistent loop was converged to 1.0×10^{-7} eV. To model one-dimensional nanowires, a tetragonal unit cell with an inter-wire distance of 20 Å was used, ensuring a minimum vacuum gap of ∼14 Å between neighboring wires. Van der Waals interactions were also examined using the DFT-D3 (BJ) method[28] but found to have no significant effect on the electronic properties. To quantify the possible strong electron correlations in Mo 4d orbitals, an on-site Coulomb repulsion parameter $U_{\rm eff}$ of 2.3 eV is extracted and used following the linear-response approach of Dudarev and Timrov *et al.*[29,30]

To evaluate thermodynamic stability, the cohesive energy $E_{\rm coh}$ per atom is calculated as

$$E_{\rm coh} = \frac{(N_{\rm Mo}E_{\rm Mo} + N_{\rm S}E_{\rm S} + N_{\rm I}E_{\rm I}) - E_{\rm total}}{N_{\rm atom}},$$

and the reaction enthalpy ΔH per unit length from the reaction $Mo_{BCC} + S_8 + I_2 \longrightarrow Mo_{12}S_9I_9 + \Delta H$, is defined as

$$\Delta H = \frac{E_{\rm Mo_{BCC}} + E_{\rm S_8} + E_{\rm I_2} - E_{\rm total}}{L},$$

CPB Online In-Press

where E_{total} is the total energy of $Mo_{12}S_9I_9$, E_{Mo}, E_{S}, and E_{I} are the energies of isolated atoms, $E_{\text{Mo}_{\text{BCC}}}$, E_{S_8}, and E_{I_2} are the energies of elemental materials, and L is the axial lattice size. $N_{\text{Mo}} = 12$, $N_{\text{S}} = 9$, $N_{\text{I}} = 9$. The reference states for the elemental constituents are explicitly the body-centered cubic (BCC) molybdenum metal crystal, an isolated molecule of the S_8 ring, and the gas-phase I_2 iodine molecule.

To evaluate the magnetocrystalline anisotropy energy (MAE) and determine the easy magnetization axis, SOC is explicitly included, and a tighter convergence criterion of 1.0×10^{-8} eV is adopted. The MAE is defined and calculated as the difference per magnetic atom between the maximal and minimal total energy when spin is aligned along the hard and easy axes, respectively, i.e.,

$$\text{MAE} = \frac{E_{\text{hard axis}} - E_{\text{easy axis}}}{N_{\text{Mo}}}.$$

Phase transition pathways and energy barriers were evaluated using the climbing-image nudged elastic band (CI-NEB) method.[31] Adopting a constant-strain protocol, the axial lattice constant c of each image is linearly interpolated between the equilibrium values of the initial and final states and kept fixed, while only atomic positions are relaxed (transverse unit cell dimensions fixed at 20 Å). Seven intermediate images were linearly interpolated and relaxed until the maximum force component perpendicular to the reaction path falls below 0.01 eV/Å. Phonon dispersion calculations were performed using the finite displacement method as implemented in Phonopy[32] with $3 \times 1 \times 1$ supercells.

3. Results and discussion

3.1. Structural motif and multistability

The calculated total energy and axial stress of the $Mo_{12}S_9I_9$ nanowire as a function of the lattice constant c_{nw} are presented in Fig. 1(a). Multiple energy minima are revealed and referred to as the P_{I} phase with $c_{\text{nw}} = 11.40$ Å, the P_{II} phase with $c_{\text{nw}} = 12.64$ Å, and the P_{III} phase with $c_{\text{nw}} = 13.80$ Å. The axial stress vanishes at the three energy minima ($c_{\text{nw}} = 11.40$ Å, 12.64 Å, and 13.80 Å).

Examining the atomic structures of the three stable or metastable phases shown in Fig. 1(b), one can see that the Mo octahedra decorated by S and I atoms and interconnected by sulfur bridges remain rather rigid, while the sulfur bridges undergo distinct and discrete changes in the Mo–S–Mo angle as strain is applied along the wire. A summary of the bond angles and Mo–S bond lengths of the Mo–S–Mo sulfur bridges is given in Table 1. From one energy minimum to another, the bond lengths changed very little, whereas the bond angles change discretely between two characteristic values: approximately 90° for "short" bridges and 150° for "long" bridges.

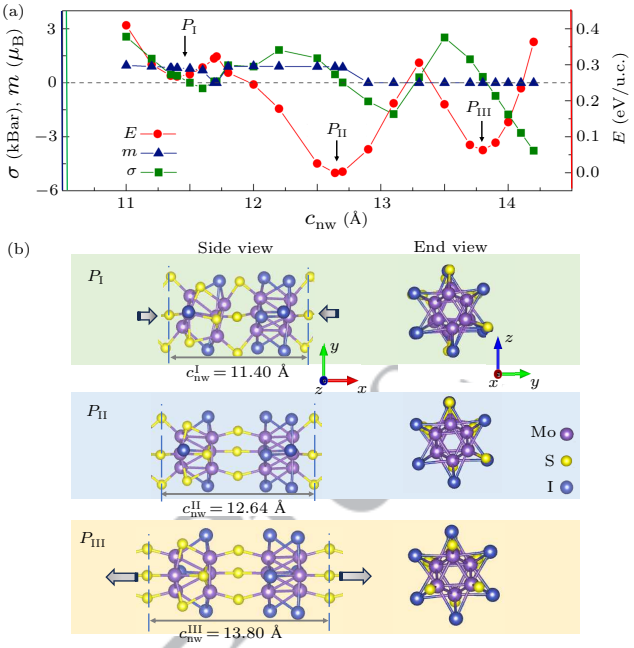


Fig. 1. Energy multistability and structural motif of $Mo_{12}S_9I_9$ nanowires. (a) Total energy (right red vertical axis), magnetic moment m (left blue vertical axis), and axial stress σ (left green vertical axis) as a function of lattice constant. Three energy minima are revealed and referred to as the P_{I} phase ($c_{\text{nw}} = 11.40$ Å), P_{II} phase ($c_{\text{nw}} = 12.64$ Å), and P_{III} phase ($c_{\text{nw}} = 13.80$ Å). (b) Side and end views of atomic structures of the three phases. The structural motif is the Mo octahedral which are decorated by I and S atoms and interconnected with each other by the sulfur bridge.

Table 1. Summary of bond angles and Mo–S bond lengths of the Mo–S–Mo sulfur bridges for the three phases. For each phase, data for the two independent bridges in the unit cell are listed separately. Angles and bond lengths are averaged over all the Mo–S bonds within each bridge.

Phase	Bridge type	Bond angle (°)	Mo–S bond length (Å)
P_{I}	"Short"	85.6	2.36
	"Short"	86.0	2.37
TS-I	"Short"	91.0	2.35
	"Short"	97.0	2.35
P_{II}	"Short"	91.3	2.35
	"Long"	148.4	2.32
TS–II	"Intermediate"	114.9	2.34
	"Long"	145.6	2.32
P_{III}	"Long"	146.7	2.29
	"Long"	146.9	2.31

More interestingly, as shown in Fig. 1(a), nonzero spin magnetic moments emerge in a wide range of c_{nw} spanning from the P_{I} phase to the P_{II} phase. The magnitude of the spin moment is approximately 0.9 μ_{B} per unit cell or roughly 0.1 μ_{B} per Mo atom, because the net spin moment arises largely from the transition metal atoms. This magnetic moment disappears in the P_{III} phase. As we discuss later in Fig. 3, both the P_{I} and P_{II} phases are semiconducting, while the P_{III} phase becomes metallic. This disappearance of magnetism marks a strain-driven phase transition between a magnetic semiconductor and a nonmagnetic metal. Considering that the P_{III} phase contains only "long" sulfur bridges, whereas the P_{I} and P_{II} phases each contain at least one "short" bridge, specifically a "short–short" configuration in P_{I} and an alternating "short–long" configu-

CPB Online In-

ration in P_{II}, this clear correlation strongly suggests that the emergence of the spin moment is intimately related to the presence of the "short" sulfur bridge configuration.

3.2. Thermodynamic and dynamical stability

MoSI nanowires were obtained by direct synthesis of the elements,[11,33] it is reasonable to evaluate the thermodynamic stability of the element reactants. The cohesive energy for all three phases, estimated using isolated atom reference energies, is ~ 4.40 eV/atom. The reaction enthalpies are 0.63 eV/Å, 0.59 eV/Å and 0.53 eV/Å for the P_{I}, P_{II} and P_{III} phases, respectively. The sizable cohesive energy and positive reaction enthalpy (exothermic reaction) both indicate that MoSI nanowires in the three phases are rather stable thermodynamically.

To assess dynamical stability, the phonon dispersion relations were calculated and shown in Fig. 2(a). Importantly, no imaginary frequencies are observed in any phonon branches in the three phases, confirming that they are all located in genuine local minima of the potential surface.

From Fig. 2(a), almost all optical phonon branches from the low- to high-frequency region of the three phases are flat. Two transverse acoustic (TA) phonon bands at the bottom also show no obvious dispersion. What is different between the phases is the longitudinal acoustic (LA) bands, highlighted in the black line, which have increasing slope (phonon velocity) from left to right, indicating increasingly deeper potentials from the P_{I} to P_{III} phase. This is consistent with the potential profile in Fig. 1(a) and also in Fig. 2(b). The extremely low phonon velocity and the frequent hybridization of the acoustic branch with multiple low-frequency optical bands may imply the possibility of very low lattice thermal conductivity in this nanowire, which could be promising for thermal insulating applications such as thermoelectricity, though a full thermal transport calculation is beyond the scope of this work.

The phase-transition path and kinetic barriers which separate the three phases were quantitatively evaluated using the CI-NEB method and are shown in Fig. 2(b). For both $P_{\mathrm{I}} \leftrightarrow P_{\mathrm{II}}$ and $P_{\mathrm{II}} \leftrightarrow P_{\mathrm{III}}$ transitions, the potential landscape is highly asymmetric. The forward barrier from P_{I} to P_{II} is as low as 0.10 eV, while the reverse barrier is 0.36 eV. For the $P_{\mathrm{II}} \leftrightarrow P_{\mathrm{III}}$ transition, the barriers are 0.30 eV and 0.23 eV. This asymmetry explains why P_{II} is readily accessible from P_{I} and P_{III} under zero-strain conditions. The depth of the P_{II} potential well is much larger than $k_{\mathrm{B}}T$ at room temperature, confirming that P_{II} is the global ground state and is dynamically and kinetically stable. The strain magnitudes of -9.8% and $+9.2\%$ that separate these phases are well within the experimentally accessible elastic limit of $Mo_6S_{9-x}I_x$ nanowires, as established by prior theoretical[18] and experimental[34] studies of this materials family.

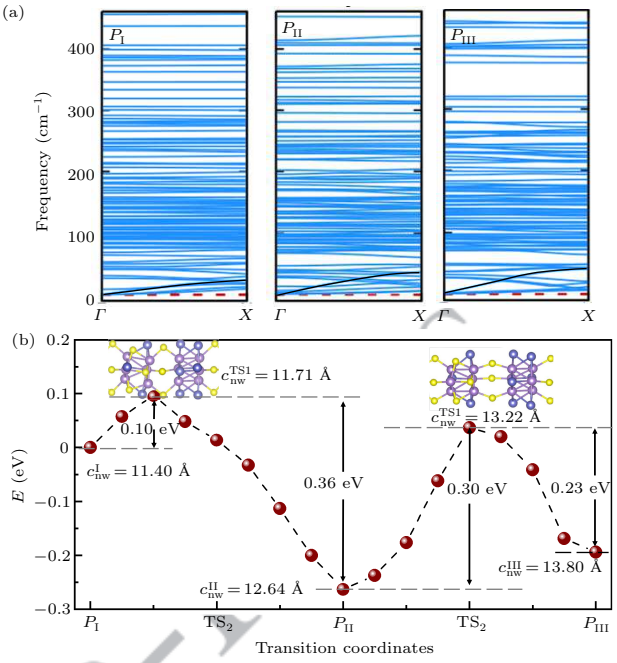


Fig. 2. (a) Phonon dispersion relation and (b) kinetic phase transition pathways of $Mo_{12}S_9I_9$ nanowires. Longitudinal acoustic (LA) phonon branches are highlighted in red line in (a). CI-NEB energy barriers and transitional structures for the sequential phase transitions are given in (b).

3.3. Electronic band structure

To understand the microscopic origin of the strain-induced magnetism observed in Fig. 1(a) and the phase transitions discussed above, we now examine the electronic band structures and density of states (DOS) of the three phases, as presented in Fig. 3. These results were obtained using the DFT + U method with an effective Hubbard parameter $U_{\mathrm{eff}} = 2.3$ eV applied to the Mo d orbitals, which properly accounts for the on-site Coulomb correlation effects of the Mo 4d electrons in these magnetic systems.

It should be noted that the ground-state P_{II} and the metastable P_{I} are magnetic semiconductors [Figs. 3(a) and 3(b)], while P_{III} is a nonmagnetic metal [Fig. 3(c)]. A key feature of the band structures in both P_{I} and P_{II} [Figs. 3(a) and 3(b)] is the exceptionally flat band dispersion near the band edges. The electronic states of the top valence band and lowest conduction band in these semiconductors are dominantly from Mo d orbitals, and the magnetic moments arise primarily from the Mo d_{xz}, d_{yz}, and d_{z^2} orbitals , as seen from the decomposed DOS on the right panel of Figs. 3(a) and 3(b). In contrast, the band near the Fermi level in P_{III} [Fig. 3(c)] is quite dispersive and the electron states are from the hybridization of Mo d and S p orbitals.

The evolution of the electronic structure across the three phases reveals a strong relevance between sulfur bridge geometry and the emergence of magnetism. The presence of a "short" sulfur bridge (with the Mo–S–Mo angle $\sim 90°$) creates an ideal geometry for d–p–d super-exchange interactions. According to the Goodenough–Kanamori rules,[35,36] a

CPB Online Ir-1

90° metal–ligand–metal bond angle favors ferromagnetic coupling. The Mo–S–Mo angles of $\sim 90°$ in the sulfur bridges of P_{I} and P_{II} satisfy this condition, explaining the robust ferromagnetism observed in these phases. In contrast, the "long" bridges in P_{III} ($\sim 150°$) approach a linear geometry, which suppresses ferromagnetic coupling. To verify this claim, we performed total energy calculations for both ferromagnetic and collinear A-type antiferromagnetic configurations for both P_{I} and P_{II}. The spin alignment between alternating Mo octahedra is antiferromagnetic in the A-type AFM configuration. The FM states are lower than the AFM states by at least 20 meV per unit cell, which is equivalent to a Curie temperature around 30 K in this nanowire system.

The narrow Mo d flat bands (bandwidth $W \sim 0.1$ eV) produce a high density of states at the Fermi level, satisfying the Stoner criterion ($U \cdot \mathrm{DOS}(E_{\mathrm{F}}) > 1$). This drives spontaneous ferromagnetic spin polarization, leading to a small but finite net magnetic moment ($\sim 0.1\ \mu_{\mathrm{B}}$/Mo) — a hallmark of weak itinerant ferromagnetism. Concurrently, the strong on-site Coulomb repulsion U (on the order of eV) in this narrow-band system, where $U/W \gg 1$, localizes electrons and opens a band gap, reminiscent of a Mott–Hubbard insulator. We therefore describe the overall metal–insulator transition as Mott–Hubbard-like (referring to the gap-opening mechanism), while the magnetic order is understood within the Stoner picture of weak itinerant ferromagnetism. These two effects synergistically coexist in the P_{I} and P_{II} phases. This instability does not occur in P_{III}, since its Fermi level lies in the center of a dispersive band where the value of DOS is very small.

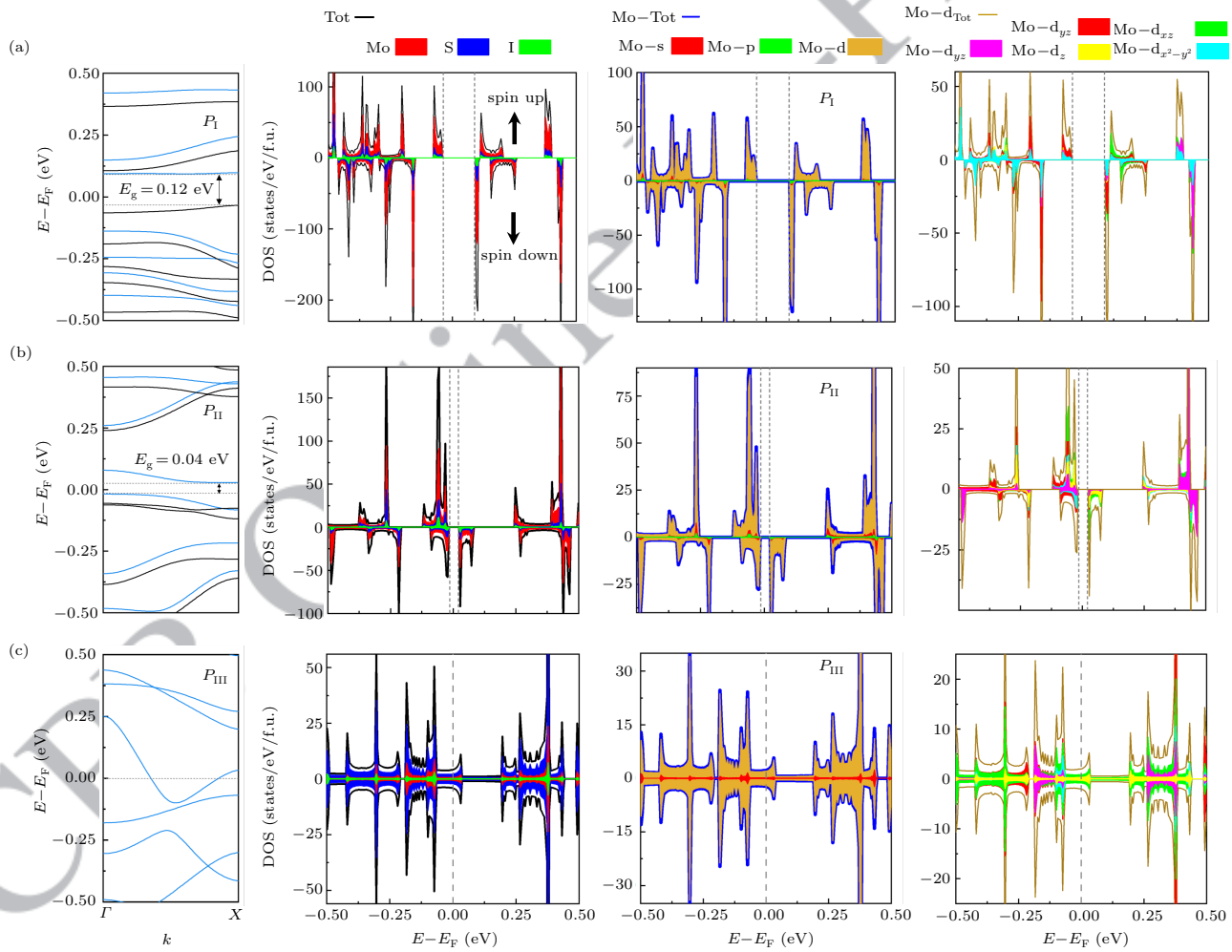


Fig. 3. Electronic band structures and density of states (DOS) of P_{I} (a), P_{II} (b), and P_{III} (c) calculated with the DFT + U method ($U_{\mathrm{eff}} = 2.3$ eV). For each panel, from left to right: electronic band structure along the nanowire axis, total DOS, atom-decomposed DOS, orbital-decomposed DOS of Mo atoms, and d-orbital-decomposed DOS of Mo atoms. The Fermi level is set at zero energy and indicated by the dashed line.

The extremely flat Mo d bands (bandwidth $W \sim 0.1$ eV) near the band edge and the emergence of a finite magnetic moment ($\sim 0.1\ \mu_{\mathrm{B}}$/Mo) already at the PBE level indicate that electronic correlations play a dominant role. In such a narrow-band limit, the kinetic energy is quenched and the system is driven into a semiconducting state by on-site Coulomb repulsion $U \sim$ eV, which is the hallmark of a strongly correlated Mott–Hubbard-like metal–insulator transition. To quantitatively account for the on-site Coulomb interactions of Mo 4d electrons, we performed DFT + U calculations with an effective Hubbard parameter $U_{\mathrm{eff}} = 2.3$ eV, as derived from linear-response theory (see Section 2). The resulting band structures

and densities of states, shown in Fig. 3, confirm that $P_{\rm I}$ and $P_{\rm II}$ are ferromagnetic semiconductors while $P_{\rm III}$ is a nonmagnetic metal. Additional tests with $U_{\rm eff}$ ranging from 0 to 4 eV show that the semiconducting nature of both $P_{\rm I}$ and $P_{\rm II}$, as well as the metallic character of $P_{\rm III}$, and their relative energy ordering remain unchanged, further validating the robustness of the Mott–Hubbard-like interpretation.

3.4. Strain-induced spin reorientation

To gain more insight into the magnetic properties of nanowires, we calculate magnetocrystalline anisotropy energies (MAEs) for $P_{\rm I}$ and $P_{\rm II}$. The spin-angle dependence of the total energy is shown in Fig. 4. Meta-stable $P_{\rm I}$ has an MAE of ~ 4.7 μeV/Mo, with its easy and hard magnetic axes at $\theta \approx 34^\circ$ and 90° with respect to the axial x-direction, respectively. Interestingly, the ground-state $P_{\rm II}$ has a larger MAE value, ~ 10.3 μeV/Mo, but with its easy and hard axes switched with respect to $P_{\rm I}$. These MAE values are comparable to that of BCC Fe (~ 4.8 μeV/Fe) but substantially smaller than those of hard magnets such as NdFeB (~ 500 μeV/Nd),[37] consistent with the moderate magnetic anisotropy expected for low-dimensional transition-metal systems.

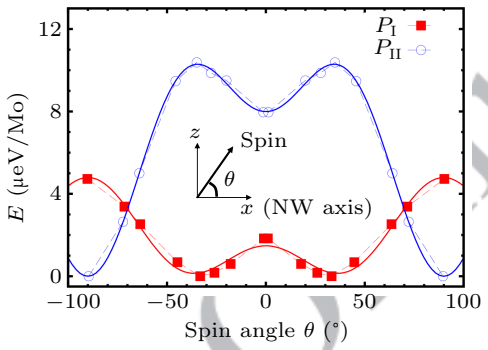


Fig. 4. Total energy of the MoSI nanowire as a function of spin orientation angle θ in the magnetic semiconducting $P_{\rm I}$ and $P_{\rm II}$ phases. The minimum energy is set to zero as reference. The angle θ is defined as the angle between the magnetic moment and the axial (x) direction. Energy is well fitted by $E(\theta) = A\sin^2\theta + B\sin^4\theta$. Meta-stable $P_{\rm I}$ has magnetic easy and hard axes at $\theta \approx 34^\circ$ and 90°, respectively, and the ground-state $P_{\rm II}$ has the easy and hard axes swapped with respect to $P_{\rm I}$.

For both phases, the magnetocrystalline anisotropy energy follows a unified expression

$$E(\theta) = E_0 + A\sin^2\theta + B\sin^4\theta,$$

where θ is the angle between the magnetic moment and the axial direction, which indicates typical uniaxial anisotropy in both phases. $A = -3.75$ μeV/Mo, $B = 7.50$ μeV/Mo for $P_{\rm I}$, and $A = 8.68$ μeV/Mo, $B = -17.36$ μeV/Mo for $P_{\rm II}$. Clearly, $P_{\rm I}$ has a canted axial magnetic anisotropy, while $P_{\rm II}$ has a perpendicular magnetic anisotropy, preferring spin aligned perpendicular to the nanowire axis. The sign reversal of A and B under strain between $P_{\rm I}$ and $P_{\rm II}$ implies strain-induced spin orientation, offering a promising route for spin-reversal storage applications.

4. Conclusion

First-principles calculations reveal that MoSI nanowires exhibit three distinct strain-responsive phases with a complex energy landscape. The global ground state ($P_{\rm II}$ at $c_{\rm nw} = 12.64$ Å) is a magnetic semiconductor. Axial compressive strain drives a transition from the global minimum ($P_{\rm II}$) to a local minimum ($P_{\rm I}$ at $c_{\rm nw} = 11.40$ Å), switching the magnetocrystalline anisotropy from perpendicular to a canted axial direction, thereby enabling a strain-controllable spin-flip channel. In contrast, tensile strain induces a Mott–Hubbard-type transition from a magnetic semiconductor to a non-magnetic metal ($P_{\rm III}$ at $c_{\rm nw} = 13.80$ Å) through tuning flat bands and strong electronic correlations. These transitions allow a single mechanical stimulus to enable strain-switchable spintronics and phase-change memory applications using MoSI nanowires. Future work should focus on experimental realization, interwire coupling in bundled geometries, and multi-field cooperative control.

Acknowledgments

Project supported by the Basic Scientific Research Project for Universities of the Department of Education of Liaoning Province (Grant No. LJ212610148025), Liaoning Provincial Science and Technology Plan Joint Program (Grant No. 2025-MSLH-444), and the National Natural Science Foundation of China (Grant No. 51702146). The numerical simulations were partially performed on the TianHe-1(A) supercomputer at the National Supercomputer Center in Tianjin, China.

References

[1] Chourasia S, Svetogorov A, Kamra A and Belzig W 2025 *Phys. Rev. B* **111** 224503
[2] Zhang S J, Zheng J J, Zhao Z W, Du S X, Lan D, Gao Z G and Wu G L 2025 *Adv. Funct. Mater.* **35** e202513762
[3] Narváez-Muñoz C, Hashemi A R, Hashemi M R, Segura L J and Ryzhakov P B 2025 *Arch. Comput. Methods Eng.* **32** 535
[4] Tao P, Guo H H, Yang T and Zhang Z D 2014 *J. Appl. Phys.* **115** 054305
[5] Dong Y, Yu Q, Yang L, Tian Z, Zhao W and Yang H 2026 *Physica B* **721** 418048
[6] Guo H, Yang T, Tao P, Wang Y and Zhang Z 2013 *J. Appl. Phys.* **113** 013709
[7] Dong B J, Guo H H, Liu Z Y, Yang T, Tao P, Tang S F, Saito R and Zhang Z D 2018 *Carbon* **131** 223
[8] Yao X H, Ji J H and Zhou X C 2025 *J. Alloys Compd.* **1044** 184458
[9] Xu R, Ye H, Wang Y Z, *et al.* 2025 *Nano Lett.* **25** 12524
[10] Shashanka H M, Saha S, Chelvane A J, Sahoo B and Anantharamaiah P N 2025 *J. Mater. Chem. C* **13** 11060
[11] Vrbanić D, Remškar M, Jesih A, Mrzel A, Umek P, Ponikvar M, Jančar B, Meden A, Novosel B, Pejovnik S, Venturini P, Coleman J C and Mihailović D 2004 *Nanotechnology* **15** 635
[12] Paglia G, Božin E S, Vengust D, Mihailovic D and Billinge S J L 2006 *Chem. Mater.* **18** 100
[13] Chung Y K, Lee W G, Chae S, Choi J Y and Huh J 2019 *Sci. Rep.* **9** 1222
[14] Žumer M, Nemanič V, Zajec B, Remškar M, Ploscaru M, Vengust D, Mrzel A and Mihailović D 2005 *Nanotechnology* **16** 1619
[15] McMullan M, Sun N J, Papakonstantinou P, Li M X, Zhou W Z and Mihailovic D 2011 *Biosens. Bioelectron.* **26** 1853

CPB Online In-Press

[16] Vilfan I and Mihailovic D 2006 *Phys. Rev. B* **74** 235411
[17] Yang T, Okano S, Berber S and Tománek D 2006 *Phys. Rev. Lett.* **96** 125502
[18] Yang T, Berber S and Tománek D 2008 *Phys. Rev. B* **77** 165426
[19] Popov I, Yang T, Berber S, Seifert G and Tománek D 2007 *Phys. Rev. Lett.* **99** 085503
[20] Kang S H, Kwon Y K and Tománek D 2010 *Phys. Rev. B* **82** 205427
[21] Kang S H, Kwon Y K and Tománek D 2010 *J. Phys.: Condens. Matter* **22** 505301
[22] Karthikeyan J, Kumar V and Murugan P 2015 *J. Phys. Chem. C* **119** 13979
[23] Kresse G and Furthmüller J 1996 *Phys. Rev. B* **54** 11169
[24] Kresse G and Joubert D 1999 *Phys. Rev. B* **59** 1758
[25] Blöchl P E 1994 *Phys. Rev. B* **50** 17953
[26] Perdew J P, Burke K and Ernzerhof M 1996 *Phys. Rev. Lett.* **77** 3865
[27] Monkhorst H J and Pack J D 1976 *Phys. Rev. B* **13** 5188
[28] Grimme S, Ehrlich S and Goerigk L 2011 *J. Comput. Chem.* **32** 1456
[29] Dudarev S L, Botton G A, Savrasov S Y, Humphreys C J and Sutton A P 1998 *Phys. Rev. B* **57** 1505
[30] Timrov I, Marzari N and Cococcioni M 2018 *Phys. Rev. B* **98** 085127
[31] Henkelman G, Uberuaga B P and Jónsson H 2000 *J. Chem. Phys.* **113** 9901
[32] Togo A and Tanaka I 2015 *Scripta Mater.* **108** 1
[33] Nicolosi V, Vrbanic D, Mrzel A, McCauley J, O'Flaherty S, Mihailovic D, Blau W J and Coleman J N 2005 *Chem. Phys. Lett.* **401** 13
[34] Kis A, Csanyi G, Vrbancic D, Mrzel A, Mihailovic D, Kulik A and Forró L 2007 *Small* **3** 1544
[35] Goodenough J B 1955 *Phys. Rev.* **100** 564
[36] Kanamori J 1959 *J. Phys. Chem. Solids* **10** 87
[37] Blundell S J 2001 *Magnetism in Condensed Matter* (Oxford University Press)

CPB Online In-Press